JOURNAL OF AIRCRAFT
Vol. 53, No. 5, September-October 2016

Optimum Wing Shape of Highly Flexible Morphing Aircraft for Improved Flight Performance

Weihua Su*
University of Alabama, Tuscaloosa, Alabama 35487-0280
Sean Shan-Min Swei†
NASA Ames Research Center, Moffett Field, California 94035
and
Guoming G. Zhu‡
Michigan State University, East Lansing, Michigan 48824

DOI: 10.2514/1.C033490

In this paper, optimum wing bending and torsion deformations are explored for a mission adaptive, highly flexible morphing aircraft. The complete highly flexible aircraft is modeled using a strain-based geometrically nonlinear beam formulation, coupled with unsteady aerodynamics and six-degree-of-freedom rigid-body motions. Since there are no conventional discrete control surfaces for trimming the flexible aircraft, the design space for searching the optimum wing geometries is enlarged. To achieve high-performance flight, the wing geometry is best tailored according to the specific flight mission needs. In this study, the steady level flight and the coordinated turn flight are considered, and the optimum wing deformations with the minimum drag at these flight conditions are searched by using a modal-based optimization procedure, subject to the trim and other constraints. The numerical study verifies the feasibility of the modal-based optimization approach, and it shows the resulting optimum wing configuration and its sensitivity under different flight profiles.

Nomenclature

a_0	=	local aerodynamic frame, with a_{0y} axis aligned with zero lift line of airfoil
a_1	=	local aerodynamic frame, with a_{1y} axis aligned with airfoil motion velocity
B	=	body reference frame
B^F, B^M	=	influence matrices for the distributed forces and moments
b	=	positions and orientations of the B frame, as a time integral of β
b_c	=	semichord of airfoil, m
C_{FF}, C_{FB}, C_{BF}, C_{BB}	=	components of generalized damping matrix
D	=	total drag of aircraft, N
d	=	distance of midchord in front of beam reference axis, m
F, M	=	forces and moments in physical frames
F_1, F_2, F_3	=	influence matrices in inflow equations with independent variables
F^{dist}, F^{pt}	=	distributed and point forces
g	=	gravitational acceleration vector, m/s^2
J	=	Jacobians
$\bar{J}$	=	trim cost function
K_{FF}	=	generalized stiffness matrix
l, m, d	=	aerodynamic loads on an airfoil
M_A	=	mass of complete aircraft, kg
M_{FF}, M_{FB}, M_{BF}, M_{BB}	=	components of generalized mass matrix
M^{dist}, M^{pt}	=	distributed and point moments
N	=	number of natural modes selected to represent aircraft deformation
N_g	=	influence matrix for gravity force
p_B, θ_B	=	position and orientation of B frame, as time integrals of v_B and ω_B, respectively
R	=	generalized load vector
R	=	range of flight, m
r	=	turn radius, m
s	=	curvilinear coordinates of beam, m
T	=	total engine thrust force, N
U	=	strain energy, J
V	=	turn speed, m/s
v_B, ω_B	=	linear and angular velocities of B frame, resolved in B frame itself
w	=	local beam reference frame defined at each node along beam reference line
x	=	complete set of variables in optimization
$\dot{y}$, $\dot{z}$	=	airfoil translational velocity components resolved in a_0 frame, m/s
α_B	=	aircraft body pitch angle, deg
$\dot{\alpha}$	=	airfoil angular velocity about a_{0x} axis, rad/s
β	=	body velocities, with translational and angular components, resolved in B frame
δ_a, δ_e, δ_r	=	aileron, elevator, and rudder deflections, deg
ε	=	elastic strain/curvature vectors
ε_x	=	extensional strain beam members
η	=	magnitudes of linear natural modes
κ_x, κ_y, κ_z	=	torsional, flat bending, and edge bending curvatures of beam members, 1/m
λ	=	inflow states, m/s

Received 8 April 2015; revision received 13 November 2015; accepted for publication 1 December 2015; published online 10 March 2016.

*Assistant Professor, Department of Aerospace Engineering and Mechanics; suw@eng.ua.edu. Senior Member AIAA.
†Research Scientist, Intelligent Systems Division; sean.s.swei@nasa.gov. Member AIAA.
‡Professor, Department of Mechanical Engineering; zhug@egr.msu.edu.

λ_0	=	inflow velocities, m/s
ρ_∞	=	air density, kg/m^3
$\mathbf{\Phi}$	=	mode shape of strain modes
φ_B	=	aircraft bank angle, deg

Subscripts

B	=	reference to B frame
BB, BF	=	components of a matrix with respect to body/flexible differential equations of motion
F	=	reference to flexible degrees of freedom
FB, FF	=	components of a matrix with respect to flexible/body differential equations of motion
hb	=	$\boldsymbol{h}$ vector with respect to motion of B frame
$h\varepsilon$	=	$\boldsymbol{h}$ vector with respect to strain ε
mc	=	midchord
pb	=	nodal position with respect to motion of B frame
$p\varepsilon$	=	nodal position with respect to strain ε
ra	=	beam reference axis
x, y, z	=	components of a reference frame
θb	=	nodal rotation with respect to motion of B frame
$\theta\varepsilon$	=	nodal rotation with respect to strain ε

I. Introduction

THE improvement of aircraft operation efficiency needs to be considered over the whole flight plan instead of a single point in the flight envelope, since the flight missions and conditions might vary during the flight. Therefore, it is natural to employ morphing wing designs so that the aircraft can be made adaptive to different flight missions and conditions. At the advent of recent development in advanced composites as well as sensor and actuator technologies, in-flight adaptive wing/aircraft morphing is now becoming a tangible goal. With the morphing technologies, aircraft performances (e.g., range, endurance, maneuverability, gust rejection, etc.) can be passively or actively tailored to different flight conditions while maintaining the flight stability. As an example, in [1,2], the roll performance of a highly flexible aircraft was tailored by using the piezoelectric actuations (e.g., microfiber composites) embedded in the skin for wing warping (bending and torsion) control. Traditionally, discrete control surfaces were used to redistribute the aerodynamic loads along the wingspan during the flight so as to tailor the aircraft performance. However, the deflection of discrete surfaces, although providing the desired lift control, may increase the aerodynamic drag. To address this issue, different techniques have been applied to explore more efficient approaches to control the wing loading, improve the aircraft performance, and reduce the drag. An effective alternative has been to introduce conformal wing/airfoil shape changes for the aerodynamic load control. FlexSys, Inc., with the support from the U.S. Air Force Research Laboratory, developed a compliant trailing-edge concept in their Mission Adaptive Compliant Wing project [3]. With a piezoelectric actuator driving the compliant morphing mechanism, it was shown in [4] that the continuous wing trailing edge was able to deflect about ± 10 deg. In [5], a cantilever wing platform was designed and experimentally tested for the camber changes with active piezoelectric actuations. In a rotorcraft application, the optimal airfoil design was studied for the control of airfoil camber [6]. Recently, in an effort to achieve a low-drag high-lift configuration, a flexible transport aircraft wing design using variable-camber continuous trailing-edge flaps to vary the wing camber was being studied at NASA Ames Research Center. The studies showed that a highly flexible wing, if elastically shaped in flight by active control of the wing twist and bending, may improve aerodynamic efficiency through drag reduction during cruise and enhanced lift performance during takeoff and landing [7]. Nguyen and Ting identified the flutter characteristics of the wing using a linear beam formulation and vortex lattice aerodynamics [8]. Their study also indicated the reduction of the flutter boundary of the wing with increased structural flexibility.

In general, the airborne intelligence, surveillance, and reconnaissance missions [9] or civilian atmospheric research [10] require vehicle platforms with high-aspect-ratio wings, resulting in highly flexible aircraft. This is because the high-altitude long-endurance flights of these aircraft demand greater aerodynamic performance. The improvement of the flight performance of the aircraft may be achieved through the high-aspect-ratio wings, as well as the lightweight, highly flexible structures. The high flexibility associated with the wing structures brings some special requirements to the formulation applied to the analysis. From the previous investigations [11], the slender wings of highly flexible aircraft may undergo large deformations under normal operating loads, exhibiting geometrically nonlinear behaviors. The structural dynamic and aeroelastic characteristics of the aircraft may change significantly due to the large deflections of their flexible wings. In addition, highly flexible aircraft usually see coupling between the low-frequency elastic modes of their slender wings and the rigid-body motions of the complete aircraft [11–15]. Therefore, the coupled effects between the large deflection due to the wing flexibility and the aeroelastic/flight dynamic characteristics of the complete aircraft must be properly accounted for in a nonlinear aeroelastic solution.

In addition to the aerodynamic platform, the lightweight structure technology is also a critical enabling path in developing high-performance aircraft. The trend in aircraft industries has been to increase the usage of composite materials in overall aircraft structure to save mass and reduce fuel burn. For example, the structure of the Boeing 787 Dreamliner consists of 80% composites by volume [16] and 50% composites by weight [17,18]. More recently, a novel aerostructure concept was under development by using lattice-based composite materials and discrete construction techniques to realize high stiffness-to-density ratio structures, enabling distributed actuation for wing shape control [19] and offering great adaptability for varying flight missions and conditions.

Various studies have been carried out to look for the optimum aircraft platform under different flight profiles, and some relevant works are summarized here. Efforts have been made to optimize the flight trajectory in order to achieve minimum fuel consumption for commercial jets [20]. With the development of new structural technologies, adaptive structures were used for performance optimization and control of flexible wings [21]. The aerodynamic shapes of different wing platforms were optimized for drag reduction using the gradient-based approach and adjoint method for sensitivity calculation [22,23]. The optimizer attained in these works was built on a Reynolds-averaged Navier–Stokes computational fluid dynamics solver. In addition, the topology of a three-dimensional (3-D) wing [24] was optimized for minimum total compliance of the wingbox, where the trim condition was considered by the changeable wing root angle of attack. A concurrent shape and topology optimization [25] of a flexible wing structure was also performed using the gradient-based optimization, achieving higher drag reduction as compared to using the sequential optimization approaches.

After all, the large wing deformation capability of highly flexible aircraft may be proactively used to improve their performance. The active aeroelastic tailoring techniques would allow aircraft designers to take advantage of the wing flexibility to create the desired wing load distribution according to the mission requirement, so as to improve overall aircraft operating efficiency and performance, without using the traditional discrete control surfaces. In doing so, one needs to understand the optimum wing bending, torsion, and camber deformations at various flight profiles. More important, the optimum wing deformations will need to be integrated with onboard flight control systems to ensure the desired wing shape is maintained at the designated flight condition.

The objective of this paper is to explore the optimum wing bending and torsion deformations (camber is not considered in the current study) of a highly flexible aircraft in seeking the most efficient flight configuration at any given flight scenario. Without modeling the builtup wing structures, a homogenized set of aircraft properties will

be used as inputs to a strain-based nonlinear aeroelastic formulation for the complete aircraft modeling. This formulation has been successfully used to design and analyze different highly flexible aircraft configurations [14,15,26]. To find the optimum wing shape among the complex space of the wing deformations, a modal-based optimization scheme will be developed, which satisfies the required trimming condition of the aircraft. In this paper, the induced drag at steady flight conditions is chosen to be the performance metric for optimization analyses. Future studies will include dynamic performance parameters (e.g., flutter instability boundary, roll maneuverability, etc.).

II. Theoretical Formulation

Solutions of the coupled aeroelasticity and flight dynamics using the strain-based geometrically nonlinear beam formulation have been discussed by Su and Cesnik [14,15,27]. An introduction of the strain-based aeroelastic equations is presented here, followed by the modal-based optimization formulation for searching the optimum wing geometries under different flight conditions.

A. System Frames

As shown in Fig. 1a, a fixed global (inertial) frame G is defined. A body frame $B(t)$ is then built in the global frame to describe the vehicle position and orientation, with $B_x(t)$ pointing to the right wing, $B_y(t)$ pointing forward, and $B_z(t)$ being the cross product of $B_x(t)$ and $B_y(t)$. The position and orientation b, as well as the time derivatives $\dot{b}$ and $\ddot{b}$ of the B frame, can be defined as

$$b = \begin{Bmatrix} p_B \\ \theta_B \end{Bmatrix} \qquad \dot{b} = \beta = \begin{Bmatrix} \dot{p}_B \\ \dot{\theta}_B \end{Bmatrix} = \begin{Bmatrix} v_B \\ \omega_B \end{Bmatrix}$$
$$\ddot{b} = \dot{\beta} = \begin{Bmatrix} \ddot{p}_B \\ \ddot{\theta}_B \end{Bmatrix} = \begin{Bmatrix} \dot{v}_B \\ \dot{\omega}_B \end{Bmatrix} \tag{1}$$

where p_B and θ_B are body position and orientation, which are both resolved in the body frame B. Note that the origin of the body frame is arbitrary in the vehicle, and it does not have to be the location of the vehicle's center of gravity.

By taking advantage of their geometry, the wing members of highly flexible aircraft are modeled as beams. Within the body frame, a local beam frame w is built at each node along the beam reference line (Fig. 1b), which is used to define the nodal position and orientation of the flexible members. Vectors $w_x(s,t)$, $w_y(s,t)$, and $w_z(s,t)$ are bases of the beam frame, for which the directions are pointing along the beam reference line, toward the leading edge (front), and normal to the wing surface, respectively, resolved in the body frame. The curvilinear beam coordinate s provides the nodal location within the body frame.

B. Elements with Constant Strains

In [28], a nonlinear beam element was introduced to model the elastic deformation of slender beams. Strain degrees (curvatures) of the beam reference line are considered as independent variables in the solution. The strain-based formulation allows simple shape functions for the element. Constant-value functions are used here. Thus, the strain vector of an element is denoted as

$$\varepsilon_e^T = \{\, \varepsilon_x \quad \kappa_x \quad \kappa_y \quad \kappa_z \,\} \tag{2}$$

where ε_x is the extensional strain; and κ_x, κ_y, and κ_z are the twist of the beam reference line, the bending about the local w_y axis, and the bending about the local w_z axis, respectively. The total strain vector of the complete aircraft is obtained by assembling the global strain vector:

$$\varepsilon^T = \{\, \varepsilon_{e1}^T \quad \varepsilon_{e2}^T \quad \varepsilon_{e3}^T \quad \dots \,\} \tag{3}$$

where ε_{ei} denotes the strain of the ith element. Transverse shear strains are not explicitly included in this equation. However, shear strain effects are included in the constitutive relation [29]. Complex geometrically nonlinear deformations can be represented by such a constant strain distribution over each element.

C. Equations of Motion

The equations of motion of the system are derived by following the principle of virtual work extended to dynamic systems (equivalent to Hamilton's principle). The total virtual work done on a beam is found by integrating the products of all internal and external forces and the corresponding virtual displacements over the volume, which is given as

$$\delta W = \int_V \delta u^T(x,y,z) f(x,y,z)\, \mathrm{d}V \tag{4}$$

where f represents general forces acting on a differential volume. This may include internal elastic forces, inertial forces, gravity forces, external distributed forces and moments, external point forces and moments, etc. The corresponding virtual displacement is δu. Following the same process described in [14], the elastic equations of motion are eventually derived as

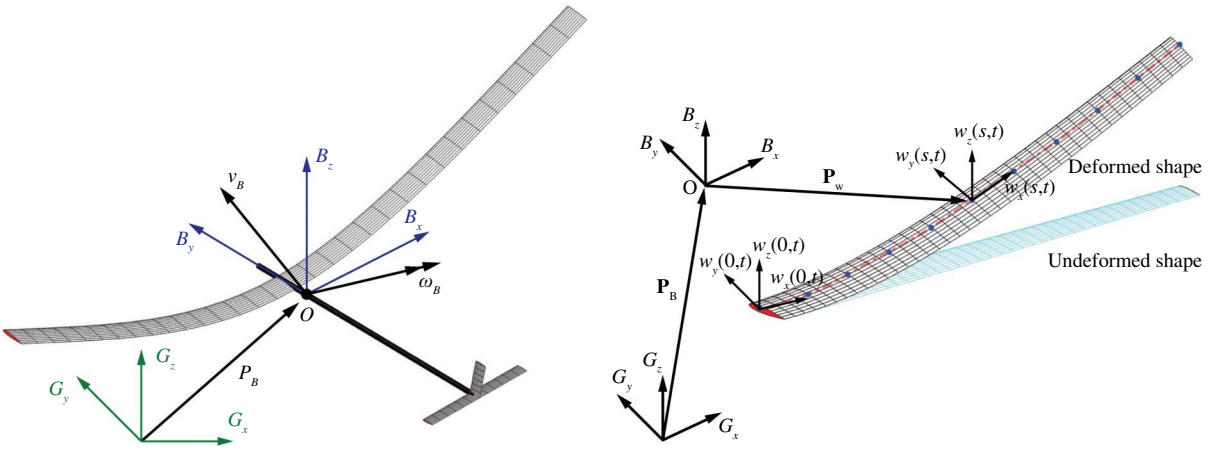

a) Global and body frames defining the rigid-body motion of aircraft

b) Flexible lifting-surface frames within body frame

Fig. 1 Basic beam reference frames.

$$\begin{bmatrix} M_{FF} & M_{FB} \\ M_{BF} & M_{BB} \end{bmatrix} \begin{Bmatrix} \ddot{\varepsilon} \\ \dot{\beta} \end{Bmatrix} + \begin{bmatrix} C_{FF} & C_{FB} \\ C_{BF} & C_{BB} \end{bmatrix} \begin{Bmatrix} \dot{\varepsilon} \\ \beta \end{Bmatrix} + \begin{bmatrix} K_{FF} & 0 \\ 0 & 0 \end{bmatrix} \begin{Bmatrix} \varepsilon \\ b \end{Bmatrix} = \begin{Bmatrix} R_F \\ R_B \end{Bmatrix} \tag{5}$$

where the components of the generalized inertia, damping, and stiffness matrices are found in [14,15]. The generalized force vector is

$$\begin{Bmatrix} R_F \\ R_B \end{Bmatrix} = \begin{Bmatrix} K_{FF}\varepsilon^0 \\ 0 \end{Bmatrix} + \begin{bmatrix} J_{h\varepsilon}^T \\ J_{hb}^T \end{bmatrix} N_g g + \begin{bmatrix} J_{p\varepsilon}^T \\ J_{pb}^T \end{bmatrix} B^F F^{\text{dist}} + \begin{bmatrix} J_{\theta\varepsilon}^T \\ J_{\theta b}^T \end{bmatrix} B^M M^{\text{dist}} + \begin{bmatrix} J_{p\varepsilon}^T \\ J_{pb}^T \end{bmatrix} F^{\text{pt}} + \begin{bmatrix} J_{\theta\varepsilon}^T \\ J_{\theta b}^T \end{bmatrix} M^{\text{pt}} \tag{6}$$

where N_g, B^F, and B^M are the influence matrices for the gravity force, distributed forces, and distributed moments, respectively, which come from the numerical integration of virtual work done by external loads along the wingspan (see [14]). The generalized force vector involves the effects from initial strains ε^0, gravitational fields g, distributed forces F^{dist}, distributed moments M^{dist}, point forces F^{pt}, and point moments M^{pt}. The aerodynamic forces and moments are considered as distributed loads. The thrust force is considered as a point follower force. All the Jacobians [$J_{h\varepsilon}, J_{p\varepsilon}, J_{\theta\varepsilon}, J_{\text{hb}}, J_{\text{pb}}$, and $J_{\theta b}$ in Eq. (6)] can be obtained from the nonlinear strain-position kinematical relationship discussed in [13,28], which links the dependent variables (nodal positions and orientations) to the independent variables (element strain and rigid-body motion). It should be noted that both the elastic member deformations and rigid-body motions are included when deriving the internal and external virtual work in [14]. Therefore, the elastic ε and rigid-body β degrees of freedom are naturally coupled. This coupling is also highlighted in Eq. (5), where the elastic deformations and the rigid-body motions are solved from the same set of equations.

D. Unsteady Aerodynamics

The distributed loads F^{dist} and M^{dist} in Eq. (6) are divided into aerodynamic loads and user-supplied loads. The unsteady aerodynamic loads used in the current study are based on the two-dimensional (2-D) finite-state inflow theory provided in [30]. The theory calculates aerodynamic loads on a thin airfoil section undergoing large motions in an incompressible inviscid subsonic flow. The lift, moment, and drag of a thin 2-D airfoil section about its midchord are given by

$$l_{\text{mc}} = \pi\rho_\infty b_c^2(-\ddot{z} + \dot{y}\dot{\alpha} - d\ddot{\alpha}) + 2\pi\rho_\infty b_c \dot{y}^2 \left[-\frac{\dot{z}}{\dot{y}} + \left(\frac{1}{2}b_c - d\right)\frac{\dot{\alpha}}{\dot{y}} - \frac{\lambda_0}{\dot{y}} \right]$$

$$m_{\text{mc}} = \pi\rho_\infty b_c^2 \left(-\frac{1}{8}b_c^2\ddot{\alpha} - \dot{y}\dot{z} - d\dot{y}\dot{\alpha} - \dot{y}\lambda_0 \right)$$

$$d_{\text{mc}} = -2\pi\rho_\infty b_c(\dot{z}^2 + d^2\dot{\alpha}^2 + \lambda_0^2 + 2d\dot{z}\dot{\alpha} + 2\dot{z}\lambda_0 + 2d\dot{\alpha}\lambda_0) \tag{7}$$

where b_c is the semichord, and d is the distance of the midchord in front of the reference axis. The quantity $-\dot{z}/\dot{y}$ is the angle of attack that consists of the contribution from both the pitching angle and the unsteady plunging motion of the airfoil. The different velocity components are shown in Fig. 2. It can be seen from Eq. (7) that only the induced drag is considered in the current study.

The inflow parameter λ_0 accounts for induced flow due to free vorticity, which is the summation of the inflow states λ as described in [30] and given by

$$\dot{\lambda} = F_1 \begin{Bmatrix} \ddot{\varepsilon} \\ \dot{\beta} \end{Bmatrix} + F_2 \begin{Bmatrix} \dot{\varepsilon} \\ \beta \end{Bmatrix} + F_3\lambda = [F_{1F} \quad F_{1B}] \begin{Bmatrix} \ddot{\varepsilon} \\ \dot{\beta} \end{Bmatrix} + [F_{2F} \quad F_{2B}] \begin{Bmatrix} \dot{\varepsilon} \\ \beta \end{Bmatrix} + F_3\lambda \tag{8}$$

The aerodynamic loads about the midchord (as defined previously) will be transferred to the wing elastic axis and rotated into the body frame for the solution of the equations of motion. To transfer the loads, one may use

$$l_{\text{ra}} = l_{\text{mc}} \qquad m_{\text{ra}} = m_{\text{mc}} + dl_{\text{mc}} \qquad d_{\text{ra}} = d_{\text{mc}} \tag{9}$$

Furthermore, the aerodynamic loads are transformed as

$$F^{\text{aero}} = C^{\text{Ba}_1} \begin{Bmatrix} 0 \\ d_{\text{ra}} \\ l_{\text{ra}} \end{Bmatrix} \qquad M^{\text{aero}} = C^{\text{Ba}_1} \begin{Bmatrix} m_{\text{ra}} \\ 0 \\ 0 \end{Bmatrix} \tag{10}$$

where C^{Ba_1} is the transformation matrix from the local aerodynamic frame to the body frame. This matrix is determined by using the instantaneous nodal orientations and has to be updated from the kinematics at each solution step and substep.

The optimization solutions will search for the optimum wing geometry based on the steady flight performances. So, the unsteady effects of the aerodynamic loads are not important at this stage. However, the unsteady effects should be included when the stability is considered in the optimization. In addition, the continuous time-domain simulations and the flight control development for the mission adaptive flights should also consider the unsteady effects.

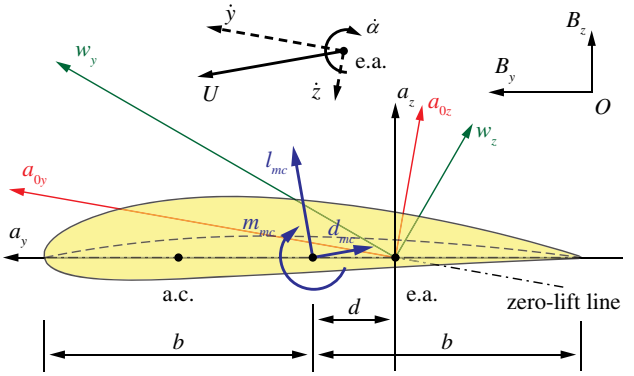

Fig. 2 Airfoil coordinate systems and velocity components.

E. Modal Representation of Aircraft Deformation

The strain field along the beam coordinate s is approximated by the combination of linear normal modes

$$\varepsilon(s,t) = \sum_{i=1}^{\infty} \Phi_i(s)\eta_i(t) \tag{11}$$

where Φ_i are the linear normal strain modes of the aircraft, and η_i are the corresponding magnitudes of the modes. To obtain the normal modes in strain, one may use the strain-based finite element equation [Eq. (5)] and perform an eigenvalue analysis with the stiffness and inertia matrices. As the stiffness matrix in Eq. (5) is singular, one can find six zero eigenvalues, which correspond to the free–free rigid-body modes. The remaining eigenvalues correspond to the coupled elastic and rigid-body modes. For the eigenvectors of these coupled modes, they generally take the following form:

$$\Phi_C = \begin{Bmatrix} \Phi_F \\ \Phi_B \end{Bmatrix} \tag{12}$$

where Φ_F and Φ_B denote the elastic and rigid-body components of the modes, respectively. Since the modal approximation in Eq. (11) only requires the elastic deformation, the rigid-body component of these modes are removed, i.e.,

$$\Phi = \Phi_F \tag{13}$$

One more note about the normal modes is that they are not necessarily obtained about the undeformed shape. One can find normal modes about a geometrically nonlinear deformation. In doing

so, the nonlinear system equations should be linearized about the deformation.

F. Trimming of Aircraft

A trim solution can be performed for both traditional aircraft with discrete control surfaces and the deformable configuration without discrete surfaces. In this study, the aircraft is trimmed at either $1g$ steady level flight or a steady coordinated turn. A scalar function can be defined for these two flight conditions:

$$\bar{J} = f^T(x) \cdot f(x) \tag{14}$$

where, for steady level flights,

$$f(x) = \begin{Bmatrix} \sum(F_y^a + F_y^g + F_y^t + F_y^u) \\ \sum(F_z^a + F_z^g + F_z^t + F_z^u) \\ \sum(M_x^a + M_x^g + M_x^t + M_x^u) \end{Bmatrix} \tag{15}$$

which includes the contributions from the aerodynamic loads on the main lifting surfaces a, gravity g, thrust t, and additional loads from control input u in the longitudinal direction. For steady coordinated turns, the following function f is used:

$$f(x) = \begin{Bmatrix} \sum(F_x^a + F_x^g + F_x^t + F_x^i + F_x^u) \\ \sum(F_y^a + F_y^g + F_y^t + F_y^i + F_y^u) \\ \sum(F_z^a + F_z^g + F_z^t + F_z^i + F_z^u) \\ \sum(M_x^a + M_x^g + M_x^t + M_x^i + M_x^u) \\ \sum(M_y^a + M_y^g + M_y^t + M_y^i + M_y^u) \\ \sum(M_z^a + M_z^g + M_z^t + M_z^i + M_z^u) \end{Bmatrix} \tag{16}$$

where the only nonzero inertial term (with the superscript i) is the centrifugal force pointing to the center of the turn path, which is given by

$$F_x^i = M_A \frac{V^2}{R} \tag{17}$$

where M_A is the total mass of the aircraft, V is the turn speed, and R is the radius of the turn path. For traditional aircraft with discrete control surfaces, the trim result for a steady level flight is found by minimizing the cost function $\bar{J}$ of Eq. (14) over the solution space using the body angle of attack α_B, the elevator deflection δ_e, and the thrust T. A Newton–Raphson scheme is used to find the local minimum of $\bar{J}$, i.e.,

$$\Delta x_k = -\left(\frac{\partial f}{\partial x}\right)_k^{-1} f_k \tag{18}$$

where

$$x_k^T = \{\, \alpha_B \quad \delta_e \quad T \,\}_k \tag{19}$$

The search variable is updated according to

$$x_{k+1} = x_k + \Delta x_k \tag{20}$$

The functional value f_{k+1} is then computed based on x_{k+1}. The process continues until the cost function $\bar{J}$ is reduced to within a prescribed tolerance. The Jacobian

$$J_f = \frac{\partial f}{\partial x} \tag{21}$$

is calculated by using finite difference. For the trim of a steady coordinated turn, Eq. (16) is used to construct the cost function $\bar{J}$, which is then minimized in the design space of the body pitch angle α_B, the bank angle φ_B, the aileron deflection δ_a, the elevator deflection δ_e, the rudder deflection δ_r, and the thrust T. It has to be noted that the trim solution should also satisfy the static equilibrium, deduced from Eq. (5) and given as

$$[K_{\mathrm{FF}}]\{\varepsilon\} = \{R^a\} + \{R^g\} + \{R^t\} + \{R^i\} + \{R^u\} \tag{22}$$

where the generalized loads on the right side of the equation correspond to the physical loads in Eq. (15) or Eq. (16).

Trimming the flexible wing aircraft (without control surfaces) follows a similar procedure. However, the control parameters of the discrete control surfaces (δ_a, δ_e, and δ_r) should be replaced by a new type of input. In this case, the control loads will be used to maintain a specific wing deformation but not to generate forces to balance the aircraft. Therefore, the corresponding terms with superscript u should be removed from Eqs. (15) and (16), resulting in

$$f(x) = \begin{Bmatrix} \sum(F_y^a + F_y^g + F_y^t) \\ \sum(F_z^a + F_z^g + F_z^t) \\ \sum(M_x^a + M_x^g + M_x^t) \end{Bmatrix} \tag{23}$$

for steady and level flights, and

$$f(x) = \begin{Bmatrix} \sum(F_x^a + F_x^g + F_x^t + F_x^i) \\ \sum(F_y^a + F_y^g + F_y^t + F_y^i) \\ \sum(F_z^a + F_z^g + F_z^t + F_z^i) \\ \sum(M_x^a + M_x^g + M_x^t + M_x^i) \\ \sum(M_y^a + M_y^g + M_y^t + M_y^i) \\ \sum(M_z^a + M_z^g + M_z^t + M_z^i) \end{Bmatrix} \tag{24}$$

for steady coordinated turns. However, the control load R^u is kept in Eq. (22) to ensure the static equilibrium of the aircraft. Since the specific control mechanism is yet to be developed, in the current study, the control load R^u will be solved from Eq. (22) as a set of generalized loads. These generalized loads are essentially the resultant bending and torsional moments along the wing, which would be produced by the control actuations. Such information can then be used for active wing shaping control through distributed actuations and for studying the tradeoff between the location and number of actuators at different flight conditions.

The focus of this paper is to explore the optimum wing geometry for better in-flight performance. To facilitate the search for the optimum wing shape, a modal-based approach will be used, which makes use of the magnitudes of natural modes in the search process.

G. Optimization Problem

Because of the large design space associated with the flexible wing aircraft, the optimum trimmed wing geometry is explored by a modal-based optimization process. If the wing deformation is represented by a truncated series of the natural modes

$$\varepsilon(s,t) = \sum_{i=1}^{N} \Phi_i(s)\eta_i(t) \tag{25}$$

then the design variables of the optimization problem become

$$x = \{\alpha_B, \varphi_B, T, \eta_1, \eta_2, \ldots, \eta_N\}^T \tag{26}$$

From flight mechanics, it is evident that the minimum drag is associated with many important flight performance metrics. For example, the flight range of a battery-powered propeller-driven airplane is derived as

$$R = \eta_t V \frac{L}{D} \frac{C}{W} \tag{27}$$

where the weight of the aircraft W is considered constant, V is the flight speed, η_t is the propulsion efficiency, and C represents the discharge capacity of the battery. The maximum range requires a minimum D/L ratio or the minimum drag with a constant lift. Therefore, the objective function in the optimization problem is defined as the drag force of the corresponding flight condition, given as

$$\min_x D = D(\alpha_B, \varphi_B, T, \eta_1, \eta_2, \ldots, \eta_N) \tag{28}$$

Note that only the induced drag is included in the current study.

Several constraints have to be satisfied by the optimum solution. The first is the trim of the aircraft:

$$C_1: \begin{cases} \sum(F_x^a + F_x^g + F_x^t + F_x^i) = 0 \\ \sum(F_y^a + F_y^g + F_y^t + F_y^i) = 0 \\ \sum(F_z^a + F_z^g + F_z^t + F_z^i) = 0 \\ \sum(M_x^a + M_x^g + M_x^t + M_x^i) = 0 \\ \sum(M_y^a + M_y^g + M_y^t + M_y^i) = 0 \\ \sum(M_z^a + M_z^g + M_z^t + M_z^i) = 0 \end{cases} \tag{29}$$

Note that this constraint is for the trim of general flights, and it can be simplified for longitudinal flights. Once the optimum wing deformation is identified, the generalized control load can be solved from the static equilibrium of Eq. (22). Obviously, the required control power cannot be too large to outperform the benefit gained from the optimum wing configuration with reduced drag. Therefore, the problem now is how much of the control power is required to maintain the optimum shape. To place a limit on the required control power, the constraint of the strain energy associated with the wing deformation is considered:

$$C_2: \left| \frac{U(x) - U_0}{U_0} \right| \le U_{\lim} \tag{30}$$

where $U(x)$ is the strain energy of the optimum wing shape, and U_0 is the strain energy of a shape that is known to be exact or close to at a trimmed condition, which can be set as a trimmed configuration with discrete control surfaces. Note that satisfying C_2 may help to avoid some unrealistic solutions that demand extremely large control power. More details about the use of C_2 will be provided in the numerical study. Furthermore, some variables should also be constrained within their search limits, such as

$$C_3: \begin{cases} \max|\kappa_x| \le \kappa_{x\,\lim} \\ \max|\kappa_y| \le \kappa_{y\,\lim} \\ \max|\kappa_z| \le \kappa_{z\,\lim} \end{cases} \tag{31}$$

$$C_4: 0 \le \varphi_B \le \varphi_{\lim} \tag{32}$$

and

$$C_5: \begin{cases} |\alpha_B| \le \alpha_{\lim} \\ 0 \le T \le T_{\lim} \end{cases} \tag{33}$$

The optimum solutions can be obtained by using MATLAB's "*fmincon*" command [31], which is a gradient-based optimizer for solving constrained nonlinear multivariable functions. To avoid numerical instability, the optimization variable x must be properly scaled. For instance, the magnitude of higher-order modes may be orders of magnitude smaller than that of lower-order modes, and such a difference in magnitude can cause numerical instability when formulating the gradient-based optimization solutions. Therefore, to improve numerical accuracy, the optimization variables x_i are all scaled with the scalar quantities d_{xi} according to

$$\hat{x}_i = x_i \cdot d_{xi} \qquad (i = 1, 2, 3, \ldots) \tag{34}$$

where d_{xi} are determined based on the initial condition of the optimization, i.e.,

$$d_{xi} = \frac{1}{x_{0i}} \tag{35}$$

The objective function and constraints are also scaled accordingly by using the reference values from the initial shape, which also helps to improve the stability of the numerical solution.

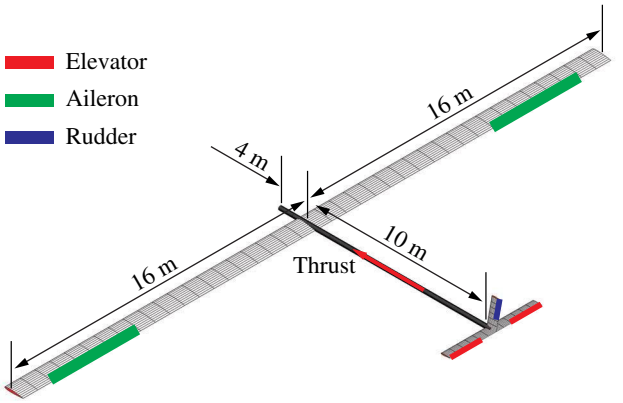

Fig. 3 Geometrical data of the baseline highly flexible aircraft.

III. Numerical Results

In this section, a highly flexible aircraft model is considered for the numerical study. The aircraft model is described first, followed by the introduction of linear modal analysis. The search for the optimum wing geometries under different flight conditions is based on the natural modes. Different optimum solutions are also compared in the study.

A. Description of the Baseline Highly Flexible Aircraft

The physical and geometrical properties of the aircraft members are shown in Fig. 3 and Table 1. The distance between the main wings and the tails is 10 m. The boom is considered rigid and massless. To keep the static stability, a point mass of 30 kg is attached to the boom at 0.75 m ahead of the main wings. The thrust force is applied at 2.5 m behind the main wings, which always points along the boom. Three sets of control surfaces are defined for the baseline vehicle, as illustrated in Fig. 3. The elevators are defined on the horizontal tails,

Table 1 Properties of the baseline highly flexible aircraft[a]

Parameter	Value	Unit
Wings		
Span	16	m
Chord	1	m
Incidence angle	2	deg
Sweep angle	0	deg
Dihedral angle	0	deg
Beam reference axis (from LE)	50	% chord
Cross-sectional c.g. (from LE)	50	% chord
Mass per span	0.75	kg · m
Rotational moment of inertia	0.1	kg · m
Torsional rigidity	1.00×10^4	N · m^2
Flat bending rigidity	2.00×10^4	N · m^2
Edge bending rigidity	4.00×10^6	N · m^2
Tails		
Span of horizontal tail	2.5	m
Span of vertical tail	1.6	m
Chord of tails	0.5	m
Incidence of horizontal tail	−3	deg
Incidence of vertical tail	0	deg
Sweep of horizontal tail	0	deg
Sweep of vertical tail	10	deg
Dihedral of horizontal tail	0	deg
Beam reference axis (from LE)	50	% chord
Cross-sectional c.g. (from LE)	50	% chord
Mass per span	0.08	kg · m
Rotational moment of inertia	0.01	kg · m
Torsional rigidity	1.00×10^4	N · m^2
Flat bending rigidity	2.00×10^4	N · m^2
Edge bending rigidity	4.00×10^6	N · m^2
Complete aircraft		
Mass	54.5	kg

[a]LE denotes "leading edge."

Table 2 Trim results of the baseline aircraft under different steady flight conditions

Flight status	Straight	Straight	Straight	Turn
Altitude, m	0	8000	20,000	20,000
Speed, m/s	6.735	10.28	25.00	20.50
Thrust, N	60.15	59.80	59.28	92.19
Body pitch angle, deg	1.28	1.27	1.26	4.44
Bank angle, deg	— —	— —	— —	14.97
Elevator angle, deg	6.76	6.76	6.75	0.572
Aileron angle, deg	— —	— —	— —	0.239
Rudder angle, deg	— —	— —	— —	−0.346
Wing tip deflection, %	32.56	32.46	32.32	32.04

running from the 1/3 span to the tip of the member. The rudder is defined on the vertical tail, also running from the 1/3 span to the tip of the member. The ailerons are defined on the main wings, running from a 70 to 90% span of the member. All the control surfaces occupy 20% chord of the corresponding aircraft member.

The main wings are divided into 10 elements in the finite element model, whereas the tail members are all divided into three elements. Previous studies [14,15,27] have shown that such a mesh with relatively few elements is sufficient for the flight performance studies of slender vehicles. The baseline aircraft can be trimmed for different flight conditions, such as the straight and level flight and steady coordinated turn in a horizontal plane at different altitudes, as listed in Table 2. The level flight speeds at different altitudes are chosen by the same dynamic pressure of the flight, whereas the turn speed is chosen by reaching a similar wingtip deflection as the level flights, with a 150 m radius of the turn path. When the aircraft is trimmed for the straight and level flight, its body orientation and wing deformation are symmetric (Fig. 4) and elevators are the only control surfaces involved in the trim. However, this symmetry generally does not hold for the steady coordinated turn (Fig. 5), where all three types of control surfaces are engaged (Table 2). The wingtip deflection, normalized by the half-span of the aircraft, for the turn flight listed in the table is also the average of the left and right wings, as the wing geometry is asymmetric in the trimmed state.

B. Natural Modes and Frequencies

Since the focus of current study is to use the flexibility of the highly flexible wings to search for the optimum wing shape with the best performance under different flight conditions, the control surfaces are "removed" from the models, whereas the wings are allowed with the full extension/bending/torsion deformations. It is expected that, with the optimum wing deformation, the vehicle's performance can be improved. In consideration of the large design space involved in searching for the optimum wing shapes, the modal-based approach is used in the study, since an arbitrary wing deformation can be represented by a linear combination of fundamental mode shapes. Therefore, the natural modes and frequencies are explored here. The mode description and the natural frequencies of the first 20 modes from the linear modal analysis are listed in Table 3. Because of the slenderness of the wings, the lower-order bending modes are coupled with the plunge and pitch modes of the rigid body. However, such coupling becomes weak and negligible for the higher-order modes.

C. Steady and Level Flight

In this study, the altitude of steady and level flight is kept at 20,000 m. The flight speed is fixed as 25 m/s. The trim results of the baseline aircraft are listed in Table 2. The elevators are removed from the aircraft model, whereas the body pitch angle and the thrust force are kept the same. Obviously, the aircraft will be unbalanced. This state is used as the initial condition of the optimization procedure, targeting to find out the new wing deformation that can minimize the drag while regaining the balance (trim). In doing so, one may carry out a series of optimizations where the possible wing deformations are represented by different numbers of modes. As the wing deformation is always symmetric for the steady and level flight, only the symmetric modes are included in the optimization. Table 4 summarizes part of the optimization results using different numbers of the symmetric modes, whereas the modal magnitude data of the optimum shapes using 3 to 10 symmetric modes are plotted in Fig. 6. From the results, it is evident that the modal-based optimization solution is converging, where the optimum (minimum) drag is about 51.3 N, whereas the drag at the initial condition is about 59.8 N. When comparing the magnitude of each mode, it can be seen that modes 1, 3, 5, and 12 contribute more than the rest of the modes. It is also of interest to note that there is a jump in the solution if a torsional mode is included, which can be observed from the results with six and seven symmetric modes. So, one may truncate the modes by selecting the first 12 modes (first seven symmetric modes) for future studies while keeping the convergence of the solution. In fact, consistent results can be obtained if one uses only modes 1, 3, 5, and 12 for the solution (see Table 4). The optimization study herein has demonstrated that the modal-based optimization solution is promising in finding the trim condition of the aircraft while

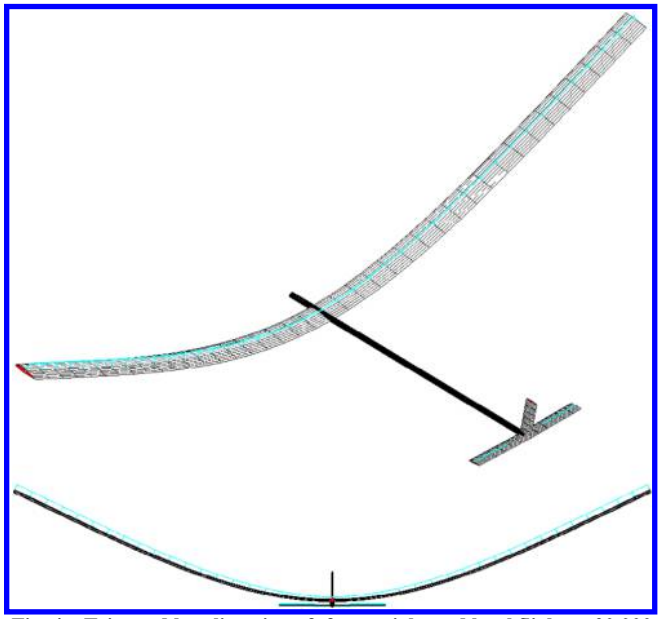

Fig. 4 Trimmed baseline aircraft for straight and level flight at 20,000 altitude.

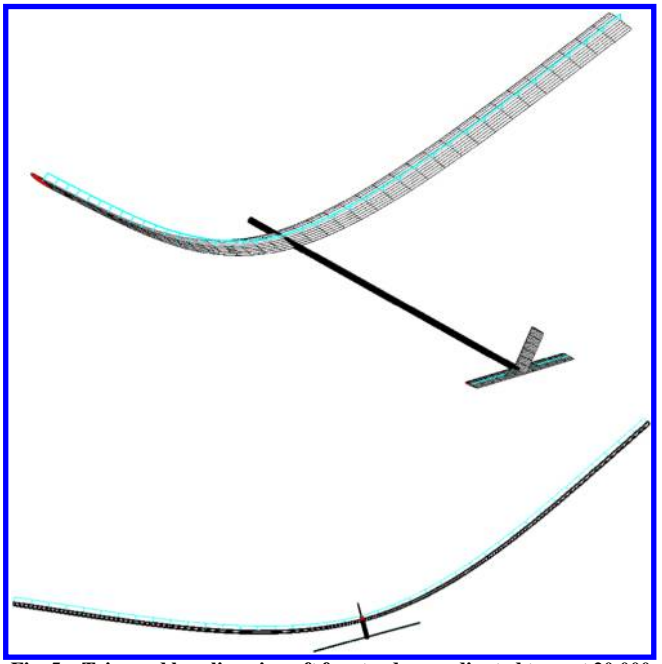

Fig. 5 Trimmed baseline aircraft for steady coordinated turn at 20,000 altitude.

Table 3 Natural modes and frequencies (in hertz) of the highly flexible aircraft about its undeformed shape[a]

	Number																			
	1	2	3	4	5	6	7	8	9	10	11	12	13	14	15	16	17	18	19	20
Rigid body	Plunge+ pitch	Roll	Plunge+ pitch	— —	Plunge+ pitch	Roll	Lead	Plunge+ pitch	Roll	Plunge	— —	— —	Roll + yaw+ side	Roll+ yaw+ side	— —	— —	— —	Roll	Lead	— —
Wing	First S flat bend	First A flat bend	Second S flat bend	First A torsion	First S torsion	Second A flat bend	First S edge bend	Third S flat bend	Third A flat bend	Fourth S flat bend	Second A torsion	Second S torsion	FourthAflatbend+ firsttailbend	Fourth A flat bend	Fifth S flat bend	Third S torsion	Third A torsion	Fifth A flat bend	Second S edge bend	Fourth S torsion
Frequency	0.4244	1.572	2.431	4.946	5.039	5.156	5.915	6.698	10.92	13.47	14.96	14.97	18.06	19.53	23.33	25.32	25.34	26.87	34.14	36.27

[a]S denotes symmetric, and A denotes antisymmetric.

searching for the optimum flight performance, which is minimum drag in this case. In addition, the modal contribution analysis presented in this paper, which identifies the modes with the most significant contributions, is intended to be used for developing the control-oriented reduced-order aircraft models.

If one converts the wing deformation from the modal magnitudes given in Table 4 to physical quantities, the resulting wing deformation is actually very small (Fig. 7). It is important to note that, to attain the solutions shown in Table 4, no constraints, other than the force and moment balance of the aircraft under the straight and level flight C_1, are applied. In other words, the optimizer has a large freedom to explore the design space defined by the natural modes to find the wing shape, as long as the external forces are balanced. Therefore, the optimum solution tends to be aggressive and difficult to achieve in reality. Actually, the uncontrolled wing geometry with the balance between the internal wing rigidity and the external gravity and aerodynamic loads will be a deep U shape, shown in Fig. 4. Hence, one will need less control authority to maintain the optimum wing shape if the shape is similar to the deep U shape. On the contrary, if the optimum wing geometry is far from the U shape, one needs a significant amount of the control authority to fight against either the aerodynamic loads or the wing stiffness in order to keep the optimum wing shape in the flight. Therefore, additional design constraints should be considered in the optimization procedure to attain a more feasible/realistic optimum wing geometry. This is achieved by introducing constraints C_2 and C_3, with the limits defined as

$$U_{\lim} = 10\% \tag{36}$$

and

$$\kappa_{x\,\lim} = 3 \times 10^{-2} \quad \kappa_{y\,\lim} = 8 \times 10^{-2} \quad \kappa_{z\,\lim} = 1 \times 10^{-3} \tag{37}$$

where the strain energy of the optimum wing shape is compared to the strain energy of the shape shown in Fig. 4, which also ensures the structural integrity of the aircraft under the combined loads. Note that the numbers in Eqs. (36) and (37) are selected to prove the optimization process is tractable, in an actual design process; however, they should be chosen according to specific aircraft models.

Table 5 summarizes the modal magnitudes and the corresponding trim parameters of the optimum wing shapes when the two constraints C_2 and C_3 are applied in addition to C_1. The results are also compared to the optimum solution with C_1 only. Note that all the solutions compared in Table 5 involve seven symmetric modes. Figures 8 and 9 illustrate the resulting optimum shapes. From Fig. 9, one can see the dominance of the first, flat bending mode (model 1), which results in the optimum wing shapes looking more like the initial wing shape but with significantly less drag. One may further compare the wing flat bending curvatures of the optimum solutions with $C_1 + C_2$ and $C_1 + C_2 + C_3$, respectively (see Fig. 10). The active constraint of C_3 in the latter case has pushed the design variable onto the boundary. The solution from $C_1 + C_2$ features bending curvatures in opposite directions along the wing, resulting in a smaller wingtip displacement, as seen in Fig. 8. It should be noted that the optimum solutions are all under a trimmed condition, whereas the initial condition is untrimmed with the removal of the elevators. In particular, as shown in Table 5, with the inclusion of constraints C_1, C_2, and C_3, the drag is reduced to 54.92 N, which is still a significant improvement from the initial drag. Figure 11 compares the generalized out-of-plane bending control loads that are required to achieve the optimum shapes from the aforementioned solutions. The generalized control loads in the other directions are significantly smaller than the out-of-plane bending loads, which are not compared herein. It can be seen that the current optimization approach, even though not finding the specific control load, is able to solve the resultant control load for the static equilibrium. The applied constraints ($C_2 + C_3$) are effectively reducing the required control power. Furthermore, the generalized control loads presented in Fig. 11 will be the guideline for future development of the distributed actuation for the wing shaping control.

Table 4 Initial and optimum (Opt.) wing shapes and trim results for steady and level flight

	Three modes		Six modes		Seven modes		Eight modes		Nine modes		Four modes[a]	
	Initial	Opt.	Initial	Opt.	Initial	Opt.	Initial	Opt.	Initial	Opt.	Initial	Opt.
Body pitch angle, deg	1.2596	2.6619	1.2596	2.6580	1.2596	2.6380	1.2596	2.6379	1.2596	2.6357	1.2596	2.6421
Thrust, N	59.2823	51.5123	59.2823	51.5205	59.2823	51.3974	59.2823	51.3976	59.2823	51.3715	59.2823	51.3895
Mode 1	1.5654	0.2212	1.5654	0.2212	1.5654	0.1904	1.5654	0.1905	1.5654	0.1862	1.5654	0.1903
Mode 3	−0.0164	−0.0161	−0.0164	−0.0161	−0.0164	−0.0161	−0.0164	−0.0161	−0.0164	−0.0161	−0.0164	−0.0160
Mode 5	0.0071	0.0021	0.0071	0.0021	0.0071	0.0020	0.0071	0.0020	0.0071	0.0020	0.0071	0.0020
Mode 7	— —	— —	0.0003	0.0003	0.0004	0.0004	0.0004	0.0004	0.0004	0.0004	— —	— —
Mode 8	— —	— —	0.0005	0.0005	0.0005	0.0005	0.0005	0.0005	0.0005	0.0005	— —	— —
Mode 10	— —	— —	−0.0002	−0.0002	−0.0002	−0.0002	−0.0002	−0.0002	−0.0002	−0.0002	— —	— —
Mode 12	—	—	—	—	−0.0014	−0.0014	−0.0014	−0.0014	−0.0014	−0.0015	−0.0014	−0.0015
Mode 15	— —	— —	— —	— —	— —	— —	0.0001	0.0001	0.0001	0.0001	— —	— —
Mode 16	— —	— —	— —	— —	— —	— —	— —	— —	0.0006	0.0006	— —	— —
Drag, N	59.84	51.46	59.84	51.47	59.84	51.34	59.84	51.34	59.84	51.32	59.84	51.33
Wingtip deflection, %	32.32	4.39	32.32	4.41	32.32	3.75	32.32	3.75	32.32	3.66	32.32	3.73
Wingtip twist, deg	4.1626	1.3165	4.1626	1.3239	4.1626	0.9712	4.1626	0.9715	4.1626	1.0400	4.1626	0.9626

[a]Including modes 1, 3, 5, and 12 only.

Table 6 lists the components of the gradient vector of the objective function D with respect to each design variable obtained at the optimum solutions. This would indicate the sensitivity of optimum drag when subject to a small perturbation in the design variables. Note that the derivative components are calculated based on the scaled design variables $\hat{x}$ so that they can be directly comparable. From Table 6, one can see that the sensitivity of the torsional modes (modes 5 and 12) and the body pitch angle are dominant at a steady level flight condition.

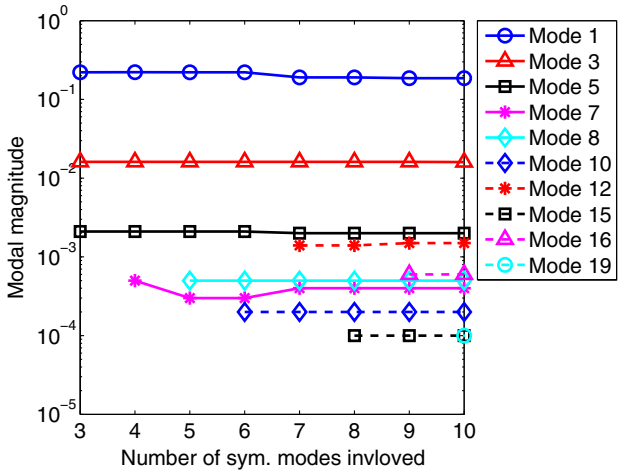

Fig. 6 Magnitudes of symmetric (sym.) modes in the optimum shape for steady and level flight.

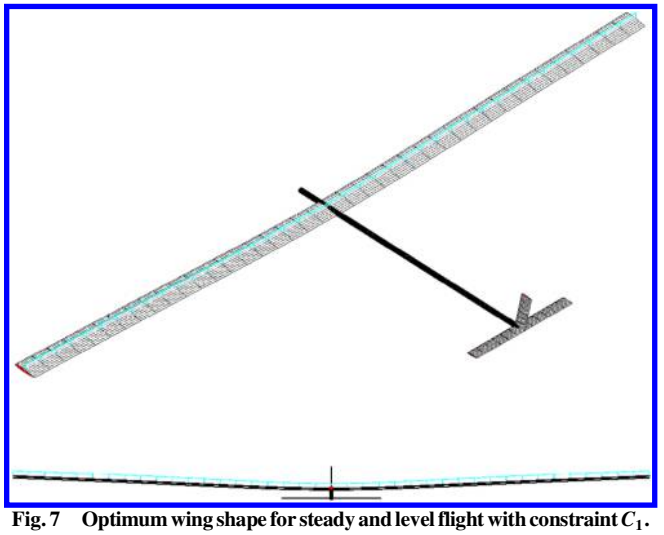

Fig. 7 Optimum wing shape for steady and level flight with constraint C_1.

D. Steady Coordinated Turn

The optimum wing geometry is also explored for the steady coordinated turn flight. The altitude is still 20,000 m, whereas the nominal turn speed is fixed at 20.50 m/s. The solution is subjected to all the aforementioned constraints during the optimization process. The antisymmetric modes must be included to represent the possible asymmetric wing geometry in a steady coordinated turn of the aircraft. Therefore, the first 12 modes are all included in the optimization solution. For a coordinated turn, it is also necessary to set a constraint on allowable bank angle C_4 to ensure the structural integrity; in this study, the limit is set as

$$\varphi_{\text{lim}} = 35 \text{ deg} \tag{38}$$

Table 7 and Fig. 12 highlight the optimum solution for the case and the comparison with the initial condition (Table 7). The wingtip deflection reported in the table is the larger value between the two wings with asymmetric deformations. It can be seen that the optimum wing geometry with the fixed turn speed is similar to the initial shape, hence similar drag. Similarly, a sensitivity analysis is performed for

Table 5 Initial and optimum wing shapes for steady and level flight with constraints

		Optimum solutions		
	Initial condition	Constraint C_1	Constraints C_1 and C_2	Constraints C_1, C_2, and C_3
Body pitch angle, deg	1.26	2.64	2.84	3.21
Thrust, N	59.28	51.40	51.67	55.00
Mode 1	1.5654	0.1904	0.5046	1.3798
Mode 3	−0.0164	−0.0161	−0.1714	−0.0708
Mode 5	0.0071	0.0020	0.0009	0.0013
Mode 7	0.0004	0.0004	0.0003	0.0004
Mode 8	0.0005	0.0005	0.0005	0.0005
Mode 10	−0.0002	−0.0002	−0.0002	−0.0002
Mode 12	−0.0014	−0.0002	−0.0001	−0.0010
Strain energy, J	439.8	10.04	395.8	395.8
Drag, N	59.84	51.34	51.61	54.92
Wingtip deflection, %	32.32	3.75	7.08	27.59
Wingtip twist, deg	4.1626	0.9712	1.0975	0.8722

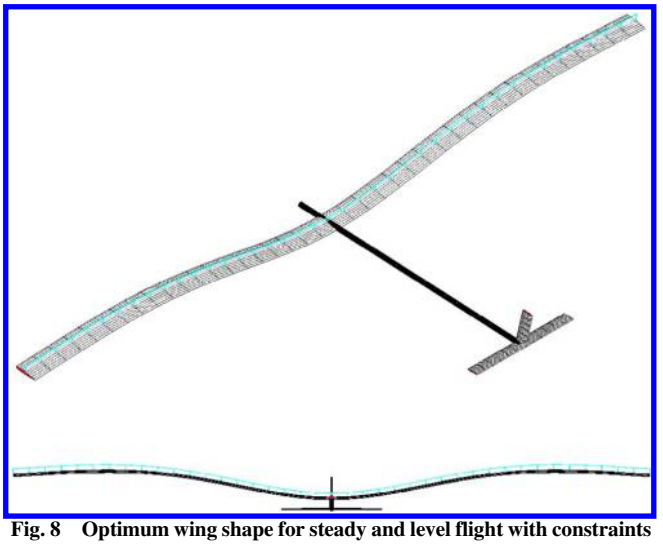

Fig. 8 Optimum wing shape for steady and level flight with constraints C_1 and C_2.

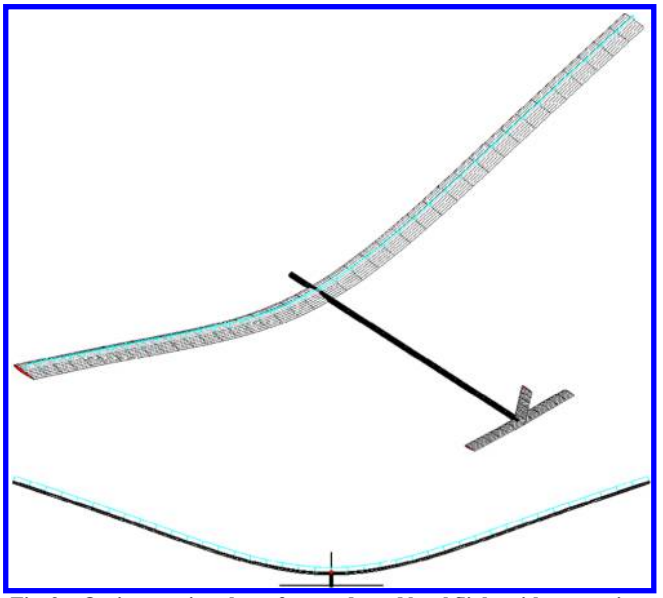

Fig. 9 Optimum wing shape for steady and level flight with constraints C_1, C_2, and C_3.

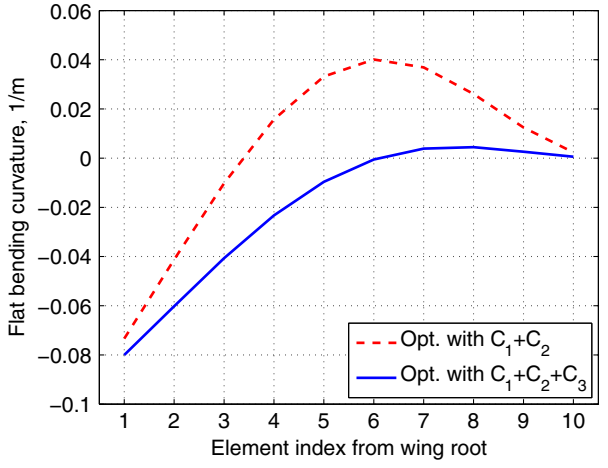

Fig. 10 Wing, flat bending curvatures of the optimum (Opt.) solutions.

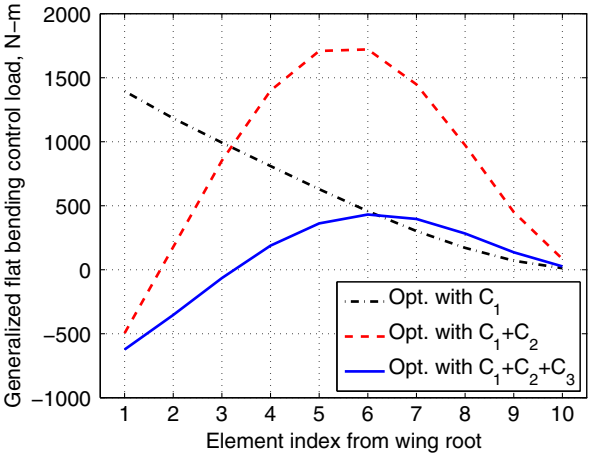

Fig. 11 Resultant flat control load distribution of the optimum solutions.

the case. Table 7 also lists the sensitivity of the drag with respect to the design variables calculated at the optimum solution. It can be seen that the most sensitive design variables are still the body pitch angle and the torsional mode (mode 5).

Table 6 Components of the gradient vector at the optimum solutions for steady level flights

$dD/d\hat{x}_i$	C_1	$C_1 + C_2$	$C_1 + C_2 + C_3$
Body pitch angle	0.3906	0.3905	0.3900
Thrust	0	0	0
Mode 1	0.0010	0.0028	−0.1637
Mode 3	0.0106	0.0086	0.0135
Mode 5	0.8487	0.8480	0.8605
Mode 7	0.0001	0.0003	−0.0002
Mode 8	−0.0020	−0.0020	−0.0021
Mode 10	−0.0001	−0.0001	−0.0001
Mode 12	0.0174	0.0156	0.0166

Table 7 Optimum wing shape and sensitivities for steady coordinated turn

	Initial condition	Optimum solution	Sensitivity $dD/d\hat{x}_i$
Body pitch angle, deg	4.44	4.51	0.8999
Bank angle, deg	14.97	15.89	0
Thrust, N	92.19	91.21	0
Mode 1	1.5529	1.4813	−0.1972
Mode 2	−0.0069	0.0005	−0.0000
Mode 3	−0.0182	−0.0188	0.0141
Mode 4	0.0000	0.0000	−0.0000
Mode 5	0.0074	0.0070	0.6237
Mode 6	0.0022	0.0025	−0.0000
Mode 7	0.0006	0.0006	−0.0003
Mode 8	0.0007	0.0007	−0.0021
Mode 9	0.0011	0.0011	−0.0000
Mode 10	−0.0002	−0.0002	−0.0001
Mode 11	0.0000	0.0000	−0.0000
Mode 12	−0.0017	−0.0016	0.0112
Strain energy, J	434.98	395.8	— —
Drag, N	91.92	90.91	— —
Maximum wingtip deflection, %	33.72	30.86	— —
Maximum wingtip twist, deg	4.2516	4.0122	— —

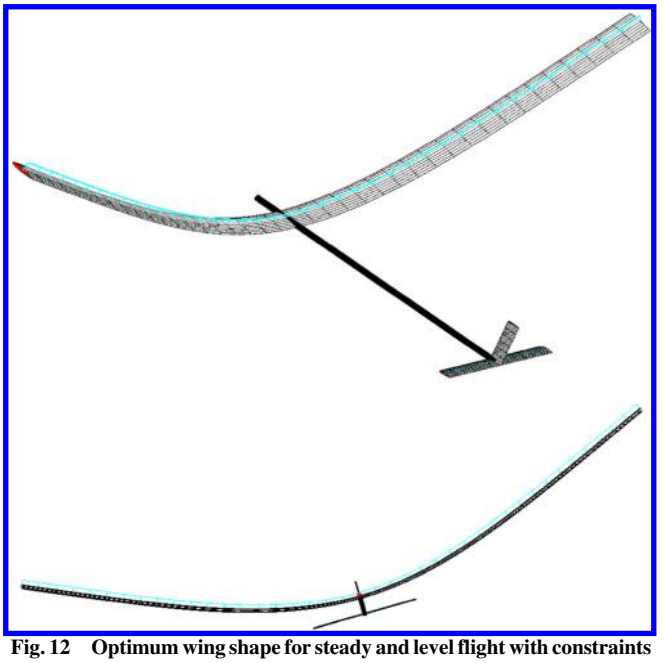

Fig. 12 Optimum wing shape for steady and level flight with constraints C_2, C_3, and C_4.

IV. Conclusions

To determine the optimum wing geometry for a mission adaptive, highly flexible morphing aircraft, the optimum wing bending and torsional deformations are explored in this paper. The goal is to search for the most efficient wing configuration that produces minimum drag at various flight profiles. The geometrically nonlinear effects of the highly flexible aircraft are modeled through a methodology that integrates a nonlinear strain-based beam model, unsteady aerodynamics, and six-degree-of-freedom rigid-body equations. With the strain-based finite element implementation of the formulation, the nonlinear wing deformations of the highly flexible aircraft are further represented by the linear normal modes. This allows for a quick and effective characterization of the contributing mode shapes to a specific wing deformation. Based on the modal representation, optimum wing geometries under different flight conditions are explored through an optimization procedure that considers the magnitude of each mode as a design variable. The objective is to minimize the drag at those flight conditions while satisfying the trimming of the aircraft and other constraints. Since the control mechanism and control loads are not available, the flapless aircraft platform and the strain energy from wing deformations are used to place a constraint on the required control authority.

Two flight conditions were considered in the current study. One was the steady level flight, and the other was the steady coordinated turn. To trim the highly flexible flapless morphing aircraft, the coupled wing bending and torsional deformations along the wingspan were used to tailor the wing load distribution. In particular, the optimum solutions showed that tailored wing twist/torsion resulted in a significant drag reduction and improved performance. Furthermore, the sensitivity analysis also indicated the importance of torsional modes.

The numerical study demonstrated the feasibility of the modal-based optimization scheme for finding the optimum wing geometry. The significance of each mode in contributing to the optimum wing geometry was also identified from the optimal solution. The sensitivity analysis indicated that further drag reduction could be effectively achieved by controlling the torsional deformation (modes). It is of importance to notice that the gradient-based optimizer *fmincon* from MATLAB was used in the study, which could only lead to a local minimum of the objective function. Even though the solution was not necessarily a global optimum, the optimization approach used in this paper rendered a rapid reduced-order model that could be used for future development of the reduced-order modal-based flight controllers. Further follow-up studies will include other flight performance metrics, such as flutter boundary, roll performance, weight penalties, etc.; and the optimum wing shapes at these flight scenarios will be determined.

Acknowledgments

The first author acknowledges sponsorship from the NASA Ames Research Center's Summer Faculty Fellowship. The work was partially supported by the NASA Aeronautics Research Mission Directorate's Team Seedling Fund and the Convergent Aeronautics Solutions project.

References

[1] Cesnik, C. E. S., and Brown, E. L., "Modeling of High Aspect Ratio Active Flexible Wings for Roll Control," *43rd AIAA/ASME/ASCE/AHS/ASC Structures, Structural Dynamics, and Materials Conference*, AIAA Paper 2002-1719, April 2002.

[2] Cesnik, C. E. S., and Brown, E. L., "Active Wing Warping Control of a Joined-Wing Airplane Configuration," *44th AIAA/ASME/ASCE/AHS/ASC Structures, Structural Dynamics, and Materials Conference*, AIAA Paper 2003-1715, April 2003.

[3] Hetrick, J., Osborn, R., Kota, S., Flick, P., and Paul, D., "Flight Testing of Mission Adaptive Compliant Wing," *48th AIAA/ASME/ASCE/AHS/ASC Structures, Structural Dynamics, and Materials Conference*, AIAA Paper 2007-1709, April 2007.

[4] Kota, S., Osborn, R., Ervin, G., Maric, D., Flick, P., and Paul, D., "Mission Adaptive Compliant Wing—Design, Fabrication and Flight Test," *NATO/RTO AVT-168 Applied Vehicle Technology Panel (AVT) Symposium on Morphing Vehicles*, Evora, Portugal, April 2009.

[5] Bilgen, O., Kochersberger, K. B., Inman, D. J., and Ohanian, O. J., "Novel, Bidirectional, Variable-Camber Airfoil via Macro-Fiber Composite Actuators," *Journal of Aircraft*, Vol. 47, No. 1, 2010, pp. 303–314. doi:10.2514/1.45452

[6] Gandhi, F., Frecker, M., and Nissly, A., "Design Optimization of a Controllable Camber Rotor Airfoil," *AIAA Journal*, Vol. 46, No. 1, 2008, pp. 142–153. doi:10.2514/1.24476

[7] Kaul, U. K., and Nguyen, N. T., "Drag Optimization Study of Variable Camber Continuous Trailing Edge Flap (VCCTEF) Using OVERFLOW," *32nd AIAA Applied Aerodynamics Conference*, AIAA Paper 2014-2444, June 2014.

[8] Nguyen, N. T., and Ting, E., "Flutter Analysis of Mission-Adaptive Wing with Variable Camber Continuous Trailing Edge Flap," *55th AIAA/ASME/ASCE/AHS/ASC Structures, Structural Dynamics, and Materials Conference*, AIAA Paper 2014-0839, Jan. 2014.

[9] Tilmann, C. P., Flick, P. M., Martin, C. A., and Love, M. H., "High-Altitude Long Endurance Technologies for SensorCraft," *NATO/RTO AVT-099 Applied Vehicle Technology Panel (AVT) Symposium on Novel and Emerging Vehicle and Vehicle Technology Concepts*, NATO Research and Technology Organization, RTO Paper MP-104-P-26, Brussels, April 2003.

[10] Noll, T. E., Ishmael, S. D., Henwood, B., Perez-Davis, M. E., Tiffany, G. C., Madura, J., Gaier, M., Brown, J. M., and Wierzbanowski, T., "Technical Findings, Lessons Learned, and Recommendations Resulting from the Helios Prototype Vehicle Mishap," *NATO/RTO AVT-145 Applied Vehicle Technology Panel (AVT) Workshop on UAV Design Processes / Design Criteria for Structures*, Florence, Italy, May 2007.

[11] Patil, M. J., Hodges, D. H., and Cesnik, C. E. S., "Nonlinear Aeroelasticity and Flight Dynamics of High-Altitude Long-Endurance Aircraft," *Journal of Aircraft*, Vol. 38, No. 1, 2001, pp. 88–94. doi:10.2514/2.2738

[12] Livne, E., and Weisshaar, T. A., "Aeroelasticity of Nonconventional Airplane Configurations—Past and Future," *Journal of Aircraft*, Vol. 40, No. 6, 2003, pp. 1047–1065. doi:10.2514/2.7217

[13] Shearer, C. M., and Cesnik, C. E. S., "Nonlinear Flight Dynamics of Very Flexible Aircraft," *Journal of Aircraft*, Vol. 44, No. 5, 2007, pp. 1528–1545. doi:10.2514/1.27606

[14] Su, W., and Cesnik, C. E. S., "Nonlinear Aeroelasticity of a Very Flexible Blended-Wing/Body Aircraft," *Journal of Aircraft*, Vol. 47, No. 5, 2010, pp. 1539–1553. doi:10.2514/1.47317

[15] Su, W., and Cesnik, C. E. S., "Dynamic Response of Highly Flexible Flying Wings," *AIAA Journal*, Vol. 49, No. 2, 2011, pp. 324–339. doi:10.2514/1.J050496

[16] Blanchard, D., "Boeing 787: A Matter of Materials—Special Report: Anatomy of a Supply Chain," *Industry Week: Advancing the Business of Manufacturing*, Nov. 2007, http://www.industryweek.com/companies-amp-executives/boeing-787-matter-materials-special-report-anatomy-supply-chain [retrieved 18 Sept. 2015].

[17] "787 Dreamliner Program Fact Sheet" http://www.boeing.com/commercial/787/ [cited 18 Sept. 2015].

[18] Hale, J., "Boeing 787 from the Ground Up," AERO Magazine, Quarter 4, 2006, pp. 17–23.

[19] Cramer, N. B., Swei, S. S.-M., Cheung, K., and Teodorescu, M., "Application of Transfer Matrix Approach to Modeling and Decentralized Control of Lattice-Based Structures," *56th AIAA/ASCE/AHS/ASC Structures, Structural Dynamics, and Materials Conference*, AIAA Paper 2015-0694, Jan. 2015.

[20] Patron, R. S. F., Berrou, Y., and Botez, R. M., "New Methods of Optimization of the Flight Profiles for Performance Database-Modeled Aircraft," *Journal of Aerospace Engineering*, Vol. 229, No. 10, 2015, pp. 1853–1867. doi:10.1177/0954410014561772

[21] Ajaj, R. M., Friswell, M. I., Dettmer, W. G., Allegri, G., and Isikveren, A. T., "Performance and Control Optimisations Using the Adaptive Torsion Wing," *Aeronautical Journal*, Vol. 116, No. 1184, 2012, pp. 1061–1077. doi:10.1017/S000192400000748X

[22] Lyu, Z., and Martins, J. R. R. A., "Aerodynamic Design Optimization Studies of a Blended-Wing-Body Aircraft," *Journal of Aircraft*, Vol. 51, No. 5, 2014, pp. 1604–1617. doi:10.2514/1.C032491

[23] Lyu, Z., Kenway, G. K. W., and Martins, J. R. R. A., "Aerodynamic Shape Optimization Investigations of the Common Research Model Wing Benchmark," *AIAA Journal*, Vol. 53, No. 4, 2015, pp. 968–985. doi:10.2514/1.J053318

[24] Dunning, P. D., Stanford, B. K., and Kim, H. A., "Coupled Aerostructural Topology Optimization Using a Level Set Method for 3-D Aircraft Wings," *Structural and Multidisciplinary Optimization*, Vol. 51, No. 5, 2015, pp. 1113–1132. doi:10.1007/s00158-014-1200-1

[25] James, K. A., Kennedy, G. J., and Martins, J. R. R. A., "Concurrent Aerostructural Topology Optimization of a Wing Box," *Computers and Structures*, Vol. 134, April 2014, pp. 1–17. doi:10.1016/j.compstruc.2013.12.007

[26] Cesnik, C. E. S., Senatore, P., Su, W., Atkins, E., and Shearer, C. M., "X-HALE: A Very Flexible Unmanned Aerial Vehicle for Nonlinear Aeroelastic Tests," *AIAA Journal*, Vol. 50, No. 12, 2012, pp. 2820–2833. doi:10.2514/1.J051392

[27] Su, W., and Cesnik, C. E. S., "Strain-Based Analysis for Geometrically Nonlinear Beams: A Modal Approach," *Journal of Aircraft*, Vol. 51, No. 3, 2014, pp. 890–903. doi:10.2514/1.C032477

[28] Su, W., and Cesnik, C. E. S., "Strain-Based Geometrically Nonlinear Beam Formulation for Modeling Very Flexible Aircraft," *International Journal of Solids and Structures*, Vol. 48, Nos. 16–17, 2011, pp. 2349–2360. doi:10.1016/j.ijsolstr.2011.04.012

[29] Palacios, R., and Cesnik, C. E. S., "Cross-Sectional Analysis of Nonhomogeneous Anisotropic Active Slender Structures," *AIAA Journal*, Vol. 43, No. 12, 2005, pp. 2624–2638. doi:10.2514/1.12451

[30] Peters, D. A., and Johnson, M. J., "Finite-State Airloads for Deformable Airfoils on Fixed and Rotating Wings," *Proceedings of Symposium on Aeroelasticity and Fluid Structure Interaction Problems, ASME Winter Annual Meeting*, AD—Vol. 44, , edited by Friedmann, P. P., and Chang, J. C. I., American Soc. of Mechanical Engineers, New York, 1994, pp. 1–28.

[31] "fmincon [online database]," MathWorks Inc., Natick, MA, http://www.mathworks.com/help/optim/ug/fmincon.html [retrieved 18 Sept. 2015].